Radiation Patterns of a Slotted-Cylinder Antenna in the Presence of an Inhomogeneous, Lossy Plasma

By Calvin T. Swift, NASA, Langley Station, Hampton, Va.

SUMMARY

A method is presented for calculating the equatorial patterns of a slot antenna on a conducting cylinder coated with a plasma which is inhomogeneous in a direction radially outward from the cylinder. The procedure consists of separating the wave equation into real and imaginary parts, and numerically integrating between appropriate boundary conditions. The solutions are coefficients of the Fourier Series which express the nature of the far field pattern. Results are presented which demonstrate the desirability of this approach to predict signal attenuation of antennas in a plasma environment.

INTRODUCTION

When a hypersonic vehicle re-enters the atmosphere, a hot gas region is formed between the body and the shock wave, thereby generating free electrons to interact with electromagnetic radiation emitted from on-board antennas. If the ionization is sufficiently strong, a radio blackout condition may occur, resulting in the disruption of communications over a large portion of the trajectory.

The electron density and collision frequency of the plasma, determined by appropriate flow field analysis, are two important quantities needed to specify the complex index of refraction, hence the nature of the interaction. In general, at any given trajectory point, the electron concentration is highly distributional, particularly in the direction normal to the vehicle. As a consequence, the propagation equations must become modified to include gradients of the index of refraction.

The geometry is another important parameter. Considerable attention has been concentrated on two models, viz. the slot on the flat ground plane[1,2,3] and the slot on the cylinder. The former has application to re-entry problems provided the curvature of the body is neglected. This theory has been developed to include losses, finite plasma dimensions, anisotropic effects and finite aperture size; however, inhomogeneous plasmas are excluded. If the wavelength is comparable to the vehicle size, the curvature of the structure and surrounding plasma must be considered. To simplify this problem, a cylinder is selected as a mathematical model; a reasonable choice since this shape represents the aft portions of many re-entry vehicles. Two source configurations are relevant to this geometry, viz. the finite aperture and the infinitely long slot. The finite slot is a more appropriate

---

1 H. Hodara, "Radiation from a Gyro-Plasma Sheathed Aperture", IRE Trans. on Antennas and Propagation, vol. AP-11, pp. 2-12; January, 1963.

2 T. Tamir and A. A. Oliner, "The Influence of Complex Waves on the Radiation Field of a Slot-Excited Plasma Layer", IRE Trans. on Antennas and Propagation, vol. AP-10, pp. 55-65; January, 1962.

3 Masayuki Omura, "Radiation Pattern of a Slit in a Ground Plane Covered by a Plasma Layer", Air Force Cambridge Research Laboratories, Hanscom Field, Mass., Rept. No. AFCRL-62-958; December, 1962.

representation of the physical picture, however, the mathematics is complete quite complicated, restricting pattern calculations to those cases where the plasma is homogeneous and non-lossy.[4,5,6] If the antenna is infinitely long, the geometry reduces to two dimensions, involving only the radial and azimuthal coordinates. The problem of the homogeneous lossy plasma has been solved in a recent report where collisions are included through the use of thin coating, and high and low frequency approximations.[7] The equations pertinent to the two-dimensional model can be extended to define interactions with inhomogeneous plasmas. However, the practical solutions of these equations, in general, are not specifiable because the plasma properties may vary arbitrarily within the shock layer. Therefore, analytical solutions[8] or WKB approximations are not realistic for many problems of interest and must be abandoned in favor of exact numerical techniques.

---

4 Charles M. Knop, "The Radiation Fields from a Circumferential Slot on a Metal Cylinder Coated with a Lossy Dielectric", IRE Trans. on Antennas and Propagation, vol. AP-9, pp. 535-545; November, 1961.

5 W. V. T. Rusch, "Radiation from a Plasma-Clad Axially-Slotted Cylinder", Electrical Engineering Department, Univ. of Southern California, Los Angeles, Calif., Rept. No. USCEC-82-201; May, 1962.

6 J. H. Harris, "Radiation Through Cylindrical Plasma Sheaths", Report prepared for Air Force Cambridge Research Laboratories, Bedford, Mass., Rept. No. AFCRL-62-976; August, 1962.

7 Dipak L. Sengupta, "The Radiation Field Produced by an Infinite Cylinder Surrounded by a Homogeneous Plasma Sheath", Radar Laboratory, The University of Michigan, Ann Arbor, Mich., Rept. No. 4563-35-T; May, 1963.

8 Cavour W. H. Yeh and Z. A. Kaprielian, "Radiation from an Axially Slotted Cylinder Coated with an Inhomogeneous Dielectric Sheath", Electrical Engineering Department, Univ. of Southern California, Los Angeles, Calif., Rept. No. USCEC-82-207; December, 1962.

One numerical approach considers the plasma as a multi-layered series of lossy homogeneous slabs.[9] This technique has been derived for convenient application to plane waves at normal incidence to a plasma slab; however, this procedure may be inadequate to describe the present problem. The boundary conditions must be applied a large number of times and calculation of Bessel function of complex arguments is required at each boundary. Since this approach seems to introduce computational difficulties, the alternative scheme of directly integrating the wave equation was chosen.[10,11]

The mechanics of the scheme is as follows: First, all the fields are properly normalized so that the boundary conditions at the air-plasma interface are expressible in terms of the known quantities (Bessel functions, index of refraction, wave number, and the radial distance to the boundary). Second, all quantities are separated into real and imaginary parts. As a result, the number of boundary conditions at the air-plasma interface are doubled, and the wave equation expands into a pair of simultaneous second-order differential equations.

---

9 T. P. Harley and G. Tyras, "Transmission of Electromagnetic Waves Through an Ionized Layer in the Presence of a Strong Magnetic Field", Proc. IRE, vol. 49, pp. 1822-1824; December, 1961.

10 J. H. Richmond, "Transmission Through Inhomogeneous Plane Layers", IRE Trans. on Antennas and Propagation, vol. AP-10, pp. 300-305; May, 1962.

11 Calvin T. Swift and John S. Evans, "Generalized Treatment of Plane Electromagnetic Waves Passing Through an Isotropic Inhomogeneous Plasma Slab at Arbitrary Angles of Incidence", National Aeronautics and Space Administration, Washington, D. C., Rept. No. NASA TR-R172; April, 1963.

Finally, the solutions of the wave equation and the excitation voltage at the conductor-plasma interface specify the unknown coefficients, hence the far field pattern.

The primary topic of this paper is the single axial slot; however, an appendix is included which describes the necessary procedures needed to calculate antenna patterns of circumferential slots.

Nomenclature

a	radius of conducting cylinder
$a\phi_o$	width of slot
b	radial extent of plasma slot
E	electric field intensity
F_{mz}	radial dependent part of electric field intensity
G_{mz}	radial dependent part of magnetic field intensity
H	magnetic field intensity
$H_m^{(2)}(x)$	Hankel function of order m and argument x
$J_m(x)$	Bessel function of order m and argument x
k_o	free space wave number
N_e	electron density, cm^{-3}
n	index of refraction
$P(\phi)$	pattern factor
r,ϕ,z	cylindrical coordinates
$\vec{u}_z$	unit vector in z direction
V_o	applied potential on slot

$$V(r) = 1 - \frac{1}{\left(\frac{\omega}{\omega_p}\right)^2 + \left(\frac{\nu}{\omega_p}\right)^2}$$

$$W(r) = \frac{\frac{\nu}{\omega_p}}{\frac{\omega}{\omega_p}} \quad \frac{1}{\left(\frac{\omega}{\omega_p}\right)^2 + \left(\frac{\nu}{\omega_p}\right)^2}$$

$Y_m(x)$ = Neumann function of order m and argument x

α attenuation coefficient

ϵ_o permittivity of free space

ϵ permittivity

μ_o permeability of free space

ν electron collision frequency

ϕ^* dummy variable representing azimuthal coordinate of the slot integration

ω propagating frequency, radians per sec.

ω_p plasma frequency = $2\pi \times 8.97 \times 10^3$ Ne

$' = d/dr$

Subscripts:

spec. specified value

r,ϕ,z vector components in the three principle directions

Superscripts:

I plasma region

II free space region

Analysis of the Axial Slot

The model shown in figure 1 consists of an infinitely long conducting cylinder into which is cut a long radiating slot of finite width. The slot is excited by a tangentially applied elmtric field, uniformaly distributed in the axial direction, but specified across the slot. An exponential factor $e^{j\omega t}$ is chosen to describe the time dependence of the fields. The complex index of refraction of the plasma surrounding the cylinder is assumed to vary only in the radial direction.

The vector wave equation which describes the propagation of the magnetic vector in the presence of inhomogeneous media is of the form:

$$\nabla^2 \vec{H} + k_o^2 n^2 \vec{H} = - \frac{\vec{\nabla} n^2}{n^2} \times \vec{\nabla} * \vec{H} \qquad (1)$$

where the complex index of refraction, n, is a function of position. In general, equation (1) expands into three rather complicated differential equations. However, the restrictions imposed by the model generate certain simplifications.

First, the problem is two dimensional, thereby requiring the derivatives of the fields with respect to the z coordinate to vanish. It also follows that

$$E_z = H_r = H_\phi = 0 \qquad (2)$$

Since the index of refraction varies only in the radial direction

$$n = n(r) \qquad (3)$$

and equation (1) reduces to:

$$\frac{1}{r}\frac{\partial}{\partial r}\left[r\frac{\partial}{\partial r}H_z^I(r,\phi)\right]+\frac{1}{r^2}\frac{\partial^2 H_z^I(r,\phi)}{\partial\phi^2}-\frac{1}{n^2}\frac{\partial n^2(r)}{\partial r}\frac{\partial H_z^I(r,\phi)}{\partial r}+k_0^2 n^2(r) H_z^I(r,\phi)=0 \quad (4)$$

$$a \le r \le b$$

Representing $H_z^I(r,\phi)$ by the complex Fourier Series:

$$H_z^I(r,\phi)=\sum_{m=-\infty}^{m=\infty} G_{mz}(r)\, e^{-jm\phi} \quad (5)$$

transforms equation (4) into the total differential equation:

$$\frac{1}{r}\frac{d}{dr}\left[r\frac{d}{dr}G_{mz}\right]-\frac{1}{n^2}\frac{dn^2}{dr}\frac{dG_{mz}}{dr}+k_0^2\left[n^2-\frac{m^2}{(k_0 r)^2}\right]G_{mz}=0 \quad (6)$$

$$a \le r \le b$$

In order to properly satisfy the boundary conditions at $r = b$ it is necessary to know the functional behavior of the wave in free space. Since the index of refraction is constant in free space the solution is:

$$H_z^{II}(r,\phi)=\sum_{m=-\infty}^{m=\infty} H_{mz}^{II}(r,\phi)=\sum_{m=-\infty}^{m=\infty} C_m H_m^{(2)}(k_0 r)\, e^{-jm\phi} \quad (7)$$

$$r \ge b$$

Where the coefficients Cm are to be determined.

The ϕ components of the electric vector are also of interest. From the relationship

$$\vec{E}=\frac{1}{j\omega\epsilon}\vec{\nabla}\times\vec{H} \quad (8)$$

the respective E_ϕ components in the plasma and in free space are given by

$$E_\phi^I = -\frac{1}{j\omega\epsilon(r)} \sum_{m=-\infty}^{m=\infty} G'_{mz}(r)\, e^{-jm\phi} \tag{9}$$

$$E_\phi^{II} = -\frac{1}{j\omega\epsilon_o} \sum_{m=-\infty}^{m=\infty} C_m H_m^{(2)\prime}(k_o r) e^{-jm\phi} \tag{10}$$

Since the tangential components of the electric and magnetic fields must be continuous at r = b the following boundary conditions must be satisfied

$$\left.\begin{aligned} H_z^I(b,\phi) &= H_z^{II}(b,\phi) \\ E_\phi^I(b,\phi) &= E_\phi^{II}(b,\phi) \end{aligned}\right\} \tag{11a}$$

And, on the surface of the cylinder, r = a, the boundary condition is given by

$$E_\phi^I(a,\phi) = E_{\phi spec.}(a,\phi) \tag{11b}$$

$E_{\phi spec.}(a,\phi)$ is the specified electric field which can be expressed in terms of the Fourier expansion[12]:

$$E_{\phi spec.}(a,\phi) = \frac{1}{2\pi} \sum_{m=-\infty}^{m=\infty} e^{-jm\phi} \int_{-\pi}^{\pi} E_\phi(a,\phi^*)\, e^{jm\phi^*}\, d\phi^* \tag{12}$$

By direct substitution the boundary conditions (equations (11a) and (11b)) become:

$$\left.\begin{aligned} C_m H_m^{(2)}(k_o b) &= G_{mz}(b) \\ C_m H_m^{(2)\prime}(k_o b) &= \frac{\epsilon_o}{\epsilon(b)} G'_{mz}(b) \end{aligned}\right\} \tag{13a}$$

$$-\frac{1}{j\omega\epsilon(a)} G'_{mz}(a) = \frac{1}{2\pi} \int_{-\pi}^{\pi} E_\phi(a,\phi^*)\, e^{jm\phi^*}\, d\phi^* \tag{13b}$$

---

[12] J. R. Wait, "Electromagnetic Radiation from Cylindrical Structures", Pergamon Press, New York, N. Y., 1959

which, for convenience, are normalized so that

$$\left.\begin{aligned} \frac{G_{mz}(b)}{C_m} &= H_m^{(2)}(k_o b) \\ \frac{G'_{mz}(b)}{C_m} &= \frac{\epsilon(b)}{\epsilon_o} H_m^{(2)\prime}(k_o b) \end{aligned}\right\} \tag{14a}$$

$$\frac{G'_{mz}(a)}{C_m} = -\,j\frac{\omega\epsilon(a)}{2\pi C_m}\int_{-\pi}^{\pi} E_\phi(a,\phi^*)\, e^{jm\phi^*}\, d\phi^* \tag{14b}$$

By means of the definition,

$$\frac{G_{mz}(r)}{C_m} = t_m(r) + j\, u_m(r) \tag{15}$$

the real and imaginary parts of equations (14) can be separated to establish values of tm, um, and their derivatives at r = b. This operation results in the re-expression of the boundary conditions in the form:

$$t_m(b) = J_m(k_o b) \tag{16}$$

$$u_m(b) = -\,Y_m(k_o b) \tag{17}$$

$$t_m'(b) = V(b)\left[-k_o J_{m+1}(k_o b) + \frac{m}{b} J_m(k_o b)\right] - W(b)\left[k_o Y_{m+1}(k_o b) - \frac{m}{b} Y_m(k_o b)\right] \tag{18}$$

$$u_m'(b) = W(b)\left[-k_o J_{m+1}(k_o b) + \frac{m}{b} J_m(k_o b)\right] + V(b)\left[k_o Y_{m+1}(k_o b) - \frac{m}{b} Y_m(k_o b)\right] \tag{19}$$

Where

$$\frac{\epsilon(r)}{\epsilon_o} = V(r) + j\, W(r) \tag{20}$$

Since the medium is a plasma, the expressions for $V(r)$ and $W(r)$ become:

$$V(r) = 1 - \frac{1}{\left[\frac{\omega}{\omega_{p(r)}}\right]^2 + \left[\frac{\nu(r)}{\omega_{p(r)}}\right]^2} \tag{21}$$

$$W(r) = \frac{\frac{\nu(r)}{\omega_{p(r)}}}{\frac{\omega}{\omega_{p(r)}}} \frac{1}{\left[\frac{\omega}{\omega_{p(r)}}\right]^2 + \left[\frac{\nu(r)}{\omega_{p(r)}}\right]^2} \tag{22}$$

Because the index, m, assumes integer values, symmetry occurs in the boundary conditions such that

$$\begin{aligned} t_{-m}(b) &= (-1)^m t_m(b) \\ u_{-m}(b) &= (-1)^m u_m(b) \\ t'_{-m}(b) &= (-1)^m t'_m(b) \\ u'_{-m}(b) &= (-1)^m u'_m(b) \end{aligned} \tag{23}$$

other than a continuity requirement on the functions and their first derivatives, $V(r)$ and $W(r)$ may vary arbitrarily. Consequently, numerical integration of the wave equation is required. In order to properly initiate the integration, equation (6) is expressed in terms of t_m and u_m through definitions (15) and (20). The left-hand side of equation (6) then separates into real and imaginary parts, each of which must independently vanish, and the result is the set of simultaneous differential equations

$$\frac{1}{r}\frac{d}{dr}\left(r\frac{dt_m}{dr}\right)-\frac{V}{V^2+W^2}\left(\frac{dV}{dr}\frac{dt_m}{dr}-\frac{dW}{dr}\frac{du_m}{dr}\right)$$

$$-\frac{W}{V^2+W^2}\left(\frac{dW}{dr}\frac{dt_m}{dr}+\frac{dV}{dr}\frac{du_m}{dr}\right)+k_0^2\left[\left(V-\frac{m^2}{(k_0r)^2}\right)t_m-Wu_m\right]=0$$

$$\frac{1}{r}\frac{d}{dr}\left(r\frac{du_m}{dr}\right)-\frac{V}{V^2+W^2}\left(\frac{dW}{dr}\frac{dt_m}{dr}+\frac{dV}{dr}\frac{du_m}{dr}\right)$$

$$+\frac{W}{V^2+W^2}\left(\frac{dV}{dr}\frac{dt_m}{dr}-\frac{dW}{dr}\frac{du_m}{dr}\right)+k_0^2\left[\left(V-\frac{m^2}{(k_0r)^2}\right)u_m+Wt_m\right]=0 \qquad (24)$$

Only positive values of m need be considered because of the recurrence relationship, equation (23).

The solutions at r = a and the boundary condition at r = a determine the unknown coefficients C_m such that

$$C_m=-j\frac{\omega\epsilon(a)}{2\pi}\int_{-\pi}^{\pi}E_\phi(a,\phi^*)e^{jm\phi^*}d\phi^*\left\{\frac{t_m'(a)-j\,u_m'(a)}{[t_m'(a)]^2+[u_m'(a)]^2}\right\} \qquad (25)$$

By substituting equation (25) into equation (7), and asymtotically expanding the Hankel function, the far-field value of $H_z^{II}(r,\phi)$ becomes:

$$H_z^{II}(r,\phi) \cong \frac{\omega\epsilon(a)}{2\pi j}\sqrt{\frac{2}{\pi k_o r}}\, e^{-j(k_o r - \frac{\pi}{4})} \sum_{m=-\infty}^{m=\infty} \left\{ \frac{t_m'(a) - j\, u_m'(a)}{[t_m'(a)]^2 + [u_m'(a)]^2} \right\} \cdot$$

$$e^{-jm(\phi - \pi/2)} \int_{-\pi}^{\pi} E_\phi(a,\phi^*)\, e^{jm\phi^*}\, d\phi^* \qquad (26)$$

The absolute value of equation (26) is normalized by dividing by $\frac{\omega\epsilon_o V_o}{2\pi a\, k_o}\sqrt{\frac{2}{\pi k_o r}}$ and results in the following expression for the far-field pattern:

$$|P_z(\phi)| = \frac{k_o}{\left(\frac{V_o}{a}\right)} \left|\frac{\epsilon(a)}{\epsilon_o}\right| \left| \sum_{m=-\infty}^{m=\infty} \left\{ \frac{t_m'(a) - j\, u_m'(a)}{[t_m'(a)]^2 + [u_m'(a)]^2} \right\} e^{-jm(\phi - \frac{\pi}{2})} \int_{-\pi}^{\pi} E_\phi(a,\phi^*)\, e^{jm\phi^*}\, d\phi^* \right| \qquad (27)$$

Thus, the antenna pattern of an infinite slot antenna (or array of [illegible] slots) of finite width in the ϕ direction is determined by solving m sets of the differential equation (24) and summing appropriately to achieve the desired convergence of equation (27). Furthermore, the equatorial pattern of finite length slots are also determined by using this method along with the proper normalization factors.

Results

Numerical integration of the propagation equations was performed on an IBM 7090 electronic data processing system by the Runge-Kutta method with an accuracy of 10^{-7} per integration. The radiator was assumed to be a line source with $E_{\phi_{spec.}} = \frac{V_0}{a}\,\delta(\phi^*)$, thus the Fourier integral in equation (27) is equal to V_0/a. $P_z(\phi)$ was computed at 10° increments in the range $0 \leq \phi \leq 90^\circ$ and 5° increments for $90^\circ < \phi \leq 180^\circ$. Free space patterns were calculated by requiring all input values of the electron density to vanish.

A free space pattern was manually computed and the agreement between these calculations and the computer results was excellent. The results of hand calculations were also compared with the numerical results for a case where region I was a homogeneous, non-lossy plasma. Again, the computational comparisons were good. As a final test, the program was checked against the analytical results of a $1/r$ electron density distribution given in figures 4 and 9 of reference 8. Although the magnitudes could not be compared, the shapes of the numerically determined patterns were identical with those of reference 8.

(a) The homogeneous plasma.- The homogeneous plasma was analyzed in order to determine general pattern behavior as a function of the various parameters; i.e., plasma frequency, collision frequency, plasma thickness, and cylinder size. Four overdense plasma frequencies in the range $0.01 \leq \omega/\omega_p \leq 0.3$, and two collision frequencies $\nu/\omega = 0.3$ and $\nu/\omega = 0.02$ were selected as representative values encountered under flight

conditions. The two plasma depths correspond to $b/a = 1.2$ and $b/a = 1.6$. Thin plasmas were chosen so that the attenuation would not be severe enough to cause the computing machine to overflow. The dimensions of the two structures are small compared to a wavelength and the free-space patterns ($k_o a = 0.52$) and $k_o a = 1.43$) are given in figure 2.

Patterns corresponding to extreme values of the plasma frequency are plotted in figure 3, and normalized so that the signal strength at $\phi = 0^o$ is 0 db. The most striking observation is the relatively small amount of pattern shift at constant plasma thickness, particularly with regard to the smaller structure. Another interesting feature is the increased forward directionality as the plasma thickness is increased.

These observations are consistent with the results of Appendix B. That is, if the summation indicated by equation (27) converges rapidly, and if the magnitude of V is large, the approximate pattern can be specified by computing the free space pattern of a line source located on a metallic cylinder of radius b and multiplying by $2\, e^{-\alpha(b-a)}$. The exact pattern attenuation at $\phi = 0^o$ is summarized in Table I, and the values of the approximate degradation factors are listed in Table II.

Computer results for the critical region $\omega/\omega_p = 1$ are plotted in figure 4. These patterns are much more dependent upon geometry and collision frequency than those for the overdense plasma, and it is difficult to discuss the general pattern trends, other than that the behavior becomes more anomalous as the collision frequency increases. It is of particular interest to note that a significant amount of radiation can be directed toward the rear of the antenna.

b. The inhomogeneous plasma.- As a means to test the error introduced by a WKB approximation (Appendix B), a linear variation of electron density at constant collision frequency was chosen to keep the manual computations simple. In each of the four cases considered, the electron density at $r = a$ and $\int_a^b d\,dr$ were assumed to be constant.

The three patterns grouped together in figure 5 are those for the homogeneous and two inhomogeneous plasmas of positive and negative gradients. The fourth pattern corresponds to an inhomogeneous plasma with a large, positive gradient. The pattern strengths computed by the approximate method of Appendix B are noted in figure 5.

It is immediately seen that the WKB method fails when reasonable gradients are introduced, thus strengthening the need of exact numerical techniques.

A more practical distribution of electron density and collision frequency is given in figure 6. The Re curve which continually increases from the shock to the body corresponds to a completely inviscid shock layer. The Re curve which has a maximum between the shock and the body is a flow profile which includes a viscous boundary layer.

The patterns are plotted in figures 7 and 8 for the two flow-field assumptions, and for $k_o a = 0.13$ and $k_o a = 0.52$. It is of interest to note that the plane wave transmission coefficients are -18.1 db and -34.8 db for the viscous and inviscid profiles, respectively.[13]

---

[13] Swift and Evans, op.cit., pp. 29-32

Conclusions

The following conclusions were noted:

1. Extreme pattern irregularities occur in the critical region $(\frac{\omega}{\omega_p} \sim 1)$ of a homogeneous plasma. The patterns appear to be sensitive to changes in geometry and collision frequency, and it is possible for much of the radiated energy to be directed behind the antenna.

2. If the homogeneous plasma is overdense, and if the radius of curvature of the structure is small compared to a wavelength, the patterns can be approximated by computing the free-space pattern of a source located on the surface of a metallic cylinder of radius b, and multiplying this pattern by $2\, e^{-\alpha(b-a)}$.

3. For values of $\frac{\omega}{\omega_p} < 1$, improved signal transmission occurs with increasing collision frequency.

4. The pattern is attenuated with decreasing values of $\frac{\omega}{\omega_p}$ and increasing thicknesses of the homogeneous plasma.

5. The approximate methods of computing patterns in the presence of an inhomogeneous plasma fail as the plasma gradients increase.

6. The amount of energy transmitted through the inhomogeneous plasma may be much greater than that predicted by plane-wave theory.

APPENDIX A

THE CIRCUMFERENTIAL SLOT

The geometry of this problem is shown in figure 1, however, the excitation of the slot is changed so that

$$E_r = E_\phi = H_z = 0 \tag{A1}$$

In this case, the entire interaction is uniquely described by the field component, E_z. The wave equation which describes the propagation of the electric vector is expressible in the form

$$\nabla^2 \vec{E} + k_0^2 n^2 \vec{E} = -\vec{\nabla}\left(\frac{\vec{\nabla} n^2}{n^2} \cdot \vec{E}\right) \tag{A2}$$

But,
$$\vec{E} = E_z(r,\phi)\,\vec{u}_z$$
$$n = n(r) \tag{A3}$$

Therefore, equation (A2) reduces to

$$\frac{1}{r}\frac{\partial}{\partial r}\left(r \frac{\partial E_z^I(r,\phi)}{\partial r}\right) + \frac{1}{r^2}\frac{\partial^2 E_z^I(r,\phi)}{\partial \phi^2} + k_0^2 n^2(r) E_z^I(r,\phi) = 0 \tag{A4}$$
$$a \le r \le b$$

Contrary to equation (4), equation (A4) does not depend upon the gradient of the complex index of refraction.

The free-space solutions of E_z and H_ϕ are:

$$E_z^{II}(r,\phi) = \sum_{m=-\infty}^{m=\infty} E_{mz}^{II}(r,\phi) = \sum_{m=-\infty}^{m=\infty} D_m H_m^{(2)}(k_0 r)\, e^{-jm\phi} \tag{A5}$$

$$H_\phi^{II}(r,\phi) = -\frac{1}{j\omega\mu_0} \sum_{m=-\infty}^{m=\infty} D_m H_m^{(2)\prime}(k_0 r)\, e^{-jm\phi} \tag{A6}$$

And in the inhomogeneous medium the solutions become:

$$E_z^I(r,\phi) = \sum_{m=-\infty}^{m=\infty} F_{mz}(r)\, e^{-jm\phi} \tag{A7}$$

$$H_\phi^I(r,\phi) = -\frac{1}{j\omega\mu_0} \sum_{m=-\infty}^{m=\infty} F_m'(r)\, e^{-jm\phi} \tag{A8}$$

At the surface of the cylinder, r = a, the field can be re-expressed in t he form

$$E_{z\,spec.}(a,\phi) = \frac{1}{2\pi} \sum_{m=-\infty}^{m=\infty} e^{-jm\phi} \int_{-\pi}^{\pi} E_z(a,\phi^*)\, e^{jm\phi^*}\, d\phi^* \tag{A9}$$

The tangential components of the fields must be continuous at the air-plasma interface, and the electric field must be a specified value at r = a. Therefore, the boundary conditions can be stated in terms of the following equations:

$$\frac{F_{mz}(b)}{D_m} = H_m^{(2)}(k_0 b) \tag{A10a}$$

$$\frac{F_{mz}'(b)}{D_m} = H_m^{(2)\prime}(k_0 b) \tag{A10b}$$

$$\frac{F_{mz}(a)}{D_m} = \frac{1}{2\pi D_m} \int_{-\pi}^{\pi} E_z(a,\phi^*)\, e^{jm\phi^*}\, d\phi^* \tag{A10c}$$

It is desirable to separate the real and imaginary parts of all the quantities involved. To accomplish this, let

$$\frac{F_{mz}(r)}{D_m} = g_m(r) + j\, S_m(r) \tag{A11}$$

As a result of equation (A11), the expression (A4) expands into the set of simultaneous differential equations:

$$\left.\begin{aligned} \frac{1}{r}\frac{d}{dr}\left(r\frac{dq_m}{dr}\right) + k_0^2\left[\left(V - \frac{m^2}{(k_0 r)^2}\right)q_m - W s_m\right] = 0 \\ \frac{1}{r}\frac{d}{dr}\left(r\frac{ds_m}{dr}\right) + k_0^2\left[\left(V - \frac{m^2}{(k_0 r)^2}\right)s_m + W q_m\right] = 0 \end{aligned}\right\} \qquad \text{(A12)}$$

As in the case of the axial slot, equations (A12) are integrated subject to the boundary conditions

$$\left.\begin{aligned} q_m(b) &= J_m(k_0 b) \\ s_m(b) &= -Y_m(k_0 b) \\ q_m'(b) &= -k_0 J_{m+1}(k_0 b) + \frac{m}{b} J_m(k_0 b) \\ s_m'(b) &= k_0 Y_{m+1}(k_0 b) - \frac{m}{b} Y_m(k_0 b) \end{aligned}\right\} \qquad \text{(A13)}$$

at $r = b$.

The solutions at $r = a$, and the boundary condition at $r = a$ (equation A10c) are sufficient to specify the pattern. Through the appropriate algebraic manipulation, the far field value of the electric field is

$$E_z^{\Pi} \cong \frac{1}{2\pi}\sqrt{\frac{2}{\pi k_0 r}}\, e^{-j\left(k_0 r - \frac{\pi}{4}\right)} \sum_{m=-\infty}^{m=\infty} \frac{\left[q_m(a) - j\, s_m(a)\right] e^{-jm\left(\phi - \frac{\pi}{2}\right)}}{\left[q_m(a)\right]^2 + \left[s_m(a)\right]^2} \cdot \qquad \text{(A14)}$$

$$\int_{-\pi}^{\pi} E_z(a, \phi^*)\, e^{jm\phi^*}\, d\phi^*$$

APPENDIX B

THE WKB APPROXIMATION

The equation which describes the propagation of electromagnetic wave through the radially varying inhomogeneous plasma was shown to be

$$\frac{1}{r}\frac{d}{dr}\left(r\frac{dG_{mz}}{dr}\right)-\frac{1}{n^2}\frac{dn^2}{dr}\frac{dG_{mz}}{dr}+k_0^2\left[n^2-\frac{m^2}{(k_0r)^2}\right]G_{mz}=0 \qquad \text{(B1)}$$

Through the substitution

$$r=e^x$$

Equation (B1) reduces to

$$\frac{d^2}{dx^2}G_{mz}-\frac{1}{n^2}\frac{dn^2}{dx}\frac{dG_{mz}}{dx}+k_0^2e^{2x}\left[n^2-\frac{m^2}{k_0^2}e^{-2x}\right]G_{mz}=0 \qquad \text{(B2)}$$

And, defining

$$g^2=k_0^2e^{2x}\left[n^2-\frac{m^2}{k_0^2}e^{-2x}\right] \qquad \text{(B3)}$$

The WKB approximation results in a solution of the form[14]

$$G_{mz}\cong n g^{-1/2}\left[C_1e^{j\int g\,dx}+C_2e^{-j\int g\,dx}\right]$$

$$=\frac{n}{k_0^{1/2}}\left[n^2-\frac{m^2}{(k_0r)^2}\right]^{-1/4}\left[C_1e^{jk_0\int_a^r\sqrt{n^2-\frac{m^2}{k_0^2r^2}}\,dr}\right.$$

$$\left.+C_2e^{-jk_0\int_a^r\sqrt{n^2-\frac{m^2}{k_0^2r^2}}\,dr}\right] \qquad \text{(B4)}$$

$$\left(\frac{1}{k_0^2}\left|\frac{3}{4}\left(\frac{1}{g^2}\frac{dg}{dx}\right)^2-\frac{1}{2}\frac{1}{g^3}\frac{d^2g}{dx^2}+\frac{1}{g^2}\left\{\frac{1}{n}\frac{d^2n}{dx^2}-2\left(\frac{1}{n}\frac{dn}{dx}\right)^2\right\}\right|<<1\right)$$

If the radius of the cylindrical structure is small compared to a wavelength, and if the plasma is overdense, the Fourier series (equation (27)) which determines the pattern converges rapidly. It is therefore reasonable to assume that

$$|v|>>\frac{m^2}{(k_0r)^2} \qquad \text{(B5)}$$

---

[14] K. G. Budden, "Radio Waves in the Ionosphere", Cambridge Univ. Press, New York, N. Y., pp. 142-143; 1961.

for the predominating modes. Equation (B4) therefore reduces to

$$G_{mz} \cong n^{1/2}\left[C_1 e^{jk_0\int_a^r n\,dr} + C_2 e^{-jk_0\int_a^r n\,dr}\right] \tag{B6}$$

and, the derivative becomes

$$G'_{mz} \cong jk_0 n^{3/2}\left[C_1 e^{jk_0\int_a^r n\,dr} - C_2 e^{-jk_0\int_a^r n\,dr}\right] \tag{B7}$$

where the gradients of the index of refraction have been ignored.

Application of the appropriate boundary conditions to equations (B6) and (B7) results in the following expression for the coefficient, c_m in equation (7) for a line source:

$$C_m = -j\frac{V_0}{a}\frac{1}{2\pi}\sqrt{n(a)n(b)}\;\frac{\omega\epsilon_0}{k_0}\left[\frac{1}{H_m^{(2)}(k_0b)\sin k_0\int_a^b n\,dr + \frac{n(b)}{k_0}H_m^{(2)\prime}(k_0b)\cos k_0\int_a^b n\,dr}\right] \tag{B8}$$

or

$$C_m \cong -j\frac{V_0}{a}\frac{1}{2\pi}\sqrt{\frac{n(a)}{n(b)}}\;\omega\epsilon_0\;\frac{1}{H_m^{(2)\prime}(k_0b)\cos\left(k_0\int_a^b n\,dr\right)}\;;\;\frac{n(b)}{k_0} >> 1 \tag{B9}$$

and, the far-field pattern becomes

$$P_z(\phi) \cong k_0\left|\sqrt{\frac{n(a)}{n(b)}}\;\frac{1}{\cos\left(k_0\int_a^b n\,dr\right)}\right|\left|\sum_{m=-\infty}^{m=\infty}\frac{e^{-jm(\phi-\frac{\pi}{2})}}{H_m^{(2)\prime}(k_0b)}\right| \tag{B10}$$

If the plasma thickness is sufficiently large, equation (B10) becomes

$$P_z(\phi) \cong 2\left|\sqrt{\frac{n(a)}{n(b)}}\right| e^{-\int_a^b \alpha\,dr}\;P_z^*(\phi) \tag{B11}$$

where $P_z^*(\phi)$ is the free-space pattern of a source on a perfectly conducting cylinder of radius b.

If the plasma is homogeneous,

$$P_z(\phi) \cong 2\, e^{-\alpha(b-a)}\, P_z^*(\phi) \qquad \text{(B12)}$$

Acknowledgment

The author expresses his thanks to Mrs. Beverly Latimer of the NASA Analytical Computing Group for her programming and computational efforts.

LIST OF ILLUSTRATIONS

TABLE II. EXPONENTIAL ATTENUATION FACTORS AS A FUNCTION OF PLASMA FREQUENCY, COLLISION FREQUENCY, BODY SIZE, AND PLASMA THICKNESS.

(a) b/a = 1.2

$$\left| \sum_{m=-\infty}^{m=\infty} \frac{e^{j\frac{m\pi}{2}}}{H_m^{(2)\prime}(k_0 b)} \Big/ \sum_{m=-\infty}^{m=\infty} \frac{e^{j\frac{m\pi}{2}}}{H_m^{(2)\prime}(k_0 a)} \right| \cong 2$$

$2\, e^{-\alpha(b-a)}$, db.

$\frac{\omega_p}{\omega}$	$\frac{\nu}{\omega} = 0.3\ k_0\ a=0.52$	$\frac{\nu}{\omega} = 0.02\ k_0\ a=0.52$	$\frac{\nu}{\omega} = 0.3\ k_0\ a=1.43$	$\frac{\nu}{\omega} = 0.02\ k_0\ a=1.43$
0.1	-2.681	-2.966	-17.908	-18.693
0.3	-23.094	-24.044	-74.047	-76.654
0.01	-81.445	-84.295	-	

(b) b/a = 1.6

$$\left| \sum_{m=-\infty}^{m=\infty} \frac{e^{j\frac{m\pi}{2}}}{H_m^{(2)\prime}(k_0 b)} \Big/ \sum_{m=-\infty}^{m=\infty} \frac{e^{j\frac{m\pi}{2}}}{H_m^{(2)\prime}(k_0 a)} \right| \cong 4.5$$

$2\, e^{-\alpha(b-a)}$, db

$\frac{\omega_p}{\omega}$	$\frac{\nu}{\omega} = 0.3\ k_0\ a=0.52$	$\frac{\nu}{\omega} = 0.02\ k_0\ a=0.52$	$\frac{\nu}{\omega} = 0.3\ k_0\ a=1.43$	$\frac{\nu}{\omega} = 0.02\ k_0\ a=1.43$
0.1	-20.0829	-20.9393	-65.7660	-68.11966
.03	-81.3256	-84.1732	-	-
.01	-	-	-	-

TABLE I. COMPUTER RESULTS AT $\phi = 0^\circ$ AS A FUNCTION OF PLASMA FREQUENCY, COLLISION FREQUENCY, BODY SIZE, AND PLASMA THICKNESS.

(a) b/a = 1.2

	Signal Strength at $\phi = 0^\circ$			
$\frac{\omega}{\omega_p}$	$\frac{\nu}{\omega} = 0.3$ $k_o a = 0.52$	$\frac{\nu}{\omega} = 0.02$ $k_o a = 0.52$	$\frac{\nu}{\omega} = 0.3$ $k_o a = 1.43$	$\frac{\nu}{\omega} = 0.02$ $k_o a = 0.43$
0.3	+0.747	+0.707	-1.421	-1.773
.1	-2.547	-2.822	-16.499	-17.389
.03	-21.712	-22.680	-72.753	-75.395
.01	-79.931	-82.785	------	------

(b) b/a = 1.6

	Signal Strength at $\phi = 0^\circ$			
$\frac{\omega}{\omega_p}$	$\frac{\nu}{\omega} = 0.3$ $k_o a = 0.52$	$\frac{\nu}{\omega} = 0.02$ $k_o a = 0.52$	$\frac{\nu}{\omega} = 0.3$ $k_o a = 1.43$	$\frac{\nu}{\omega} = 0.02$ $k_o a = 1.43$
0.3	-0.827	-1.202	-14.844	-15.939
.1	-16.996	-17.95	-63.257	-65.748
.03	-78.057	-80.936	---	---
.01	---	---	---	---

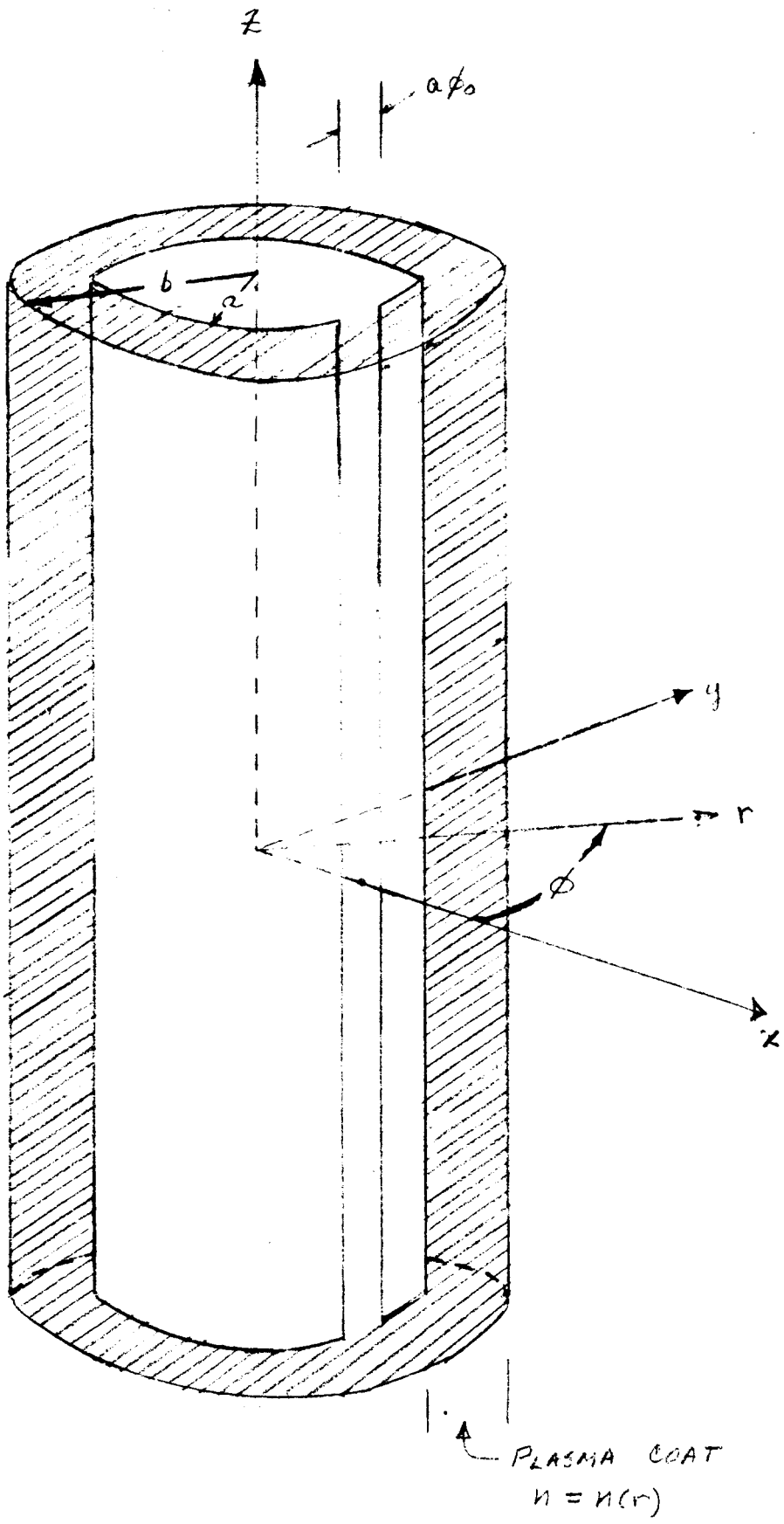

Fig. 1

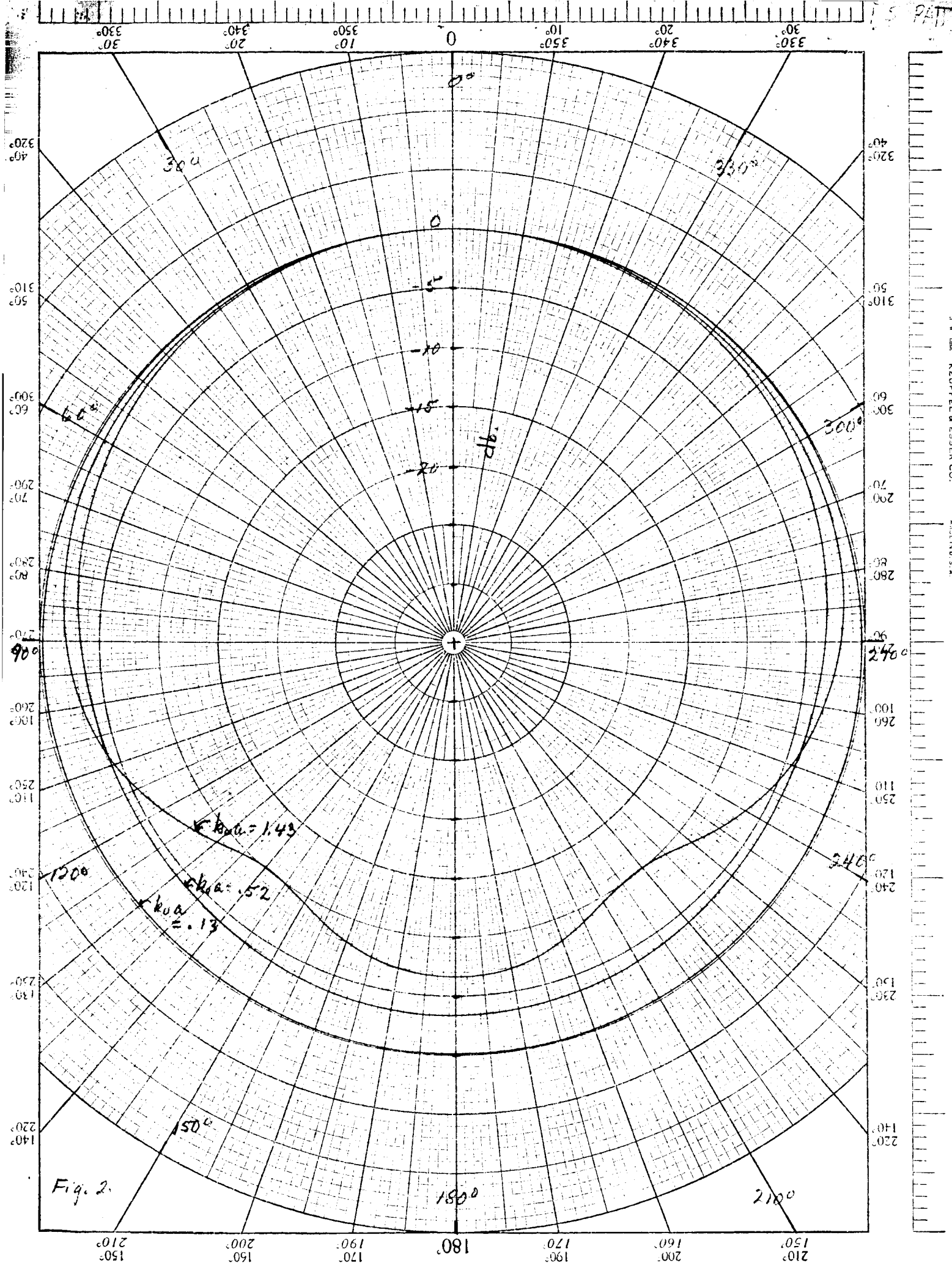
0°
30°
60°
90°
120°
150°
180°
210°
240°
270°
300°
330°
0
-5
-10
-15
-20
db
ka = 1.43
ka = .52
ka = .13
POLAR CO-ORDINATE
KEUFFEL & ESSER CO.
359-31G

Fig. 2.

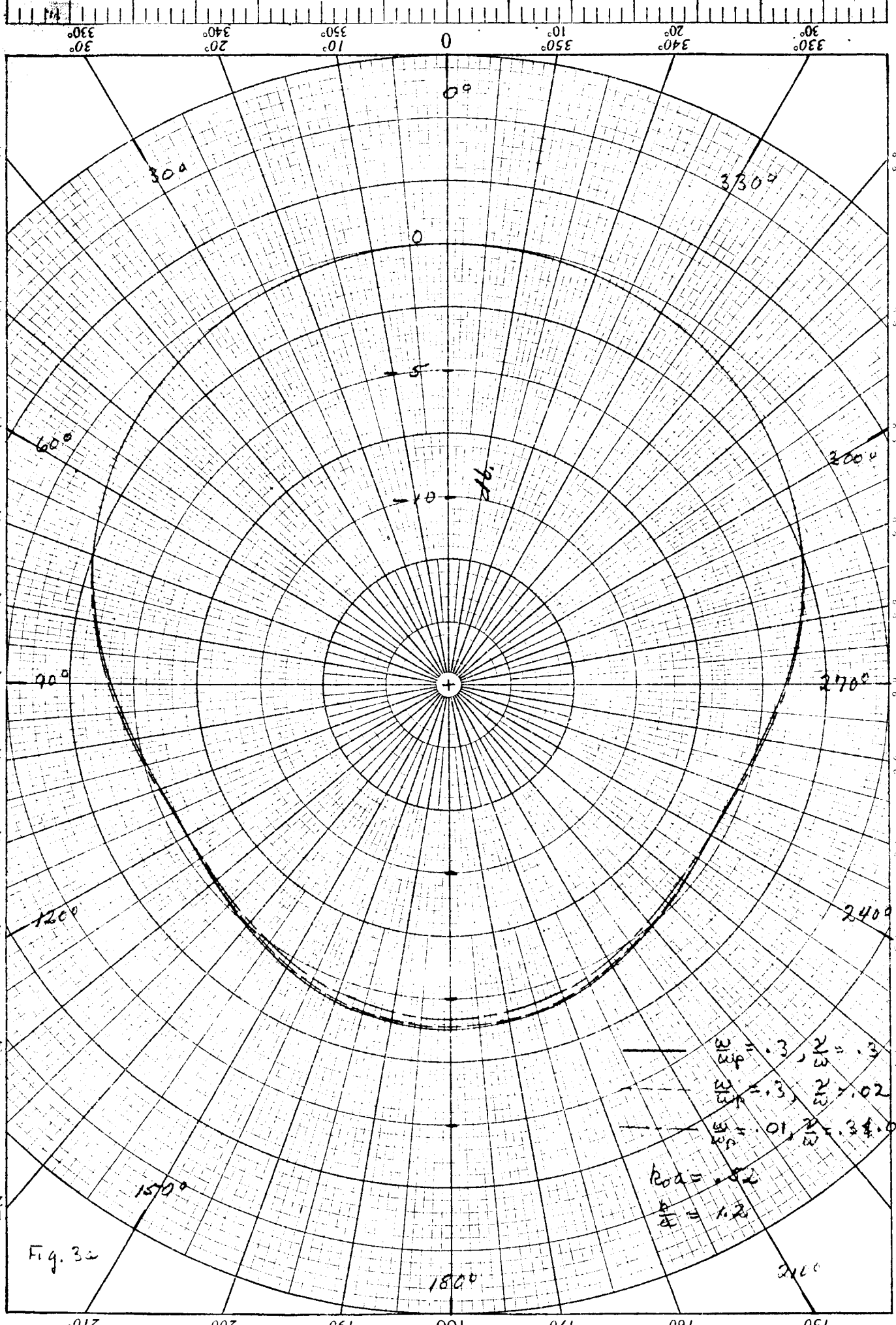

Fig. 3a

POLAR CO-ORDINATE
KEUFFEL & ESSER CO.
359-31G

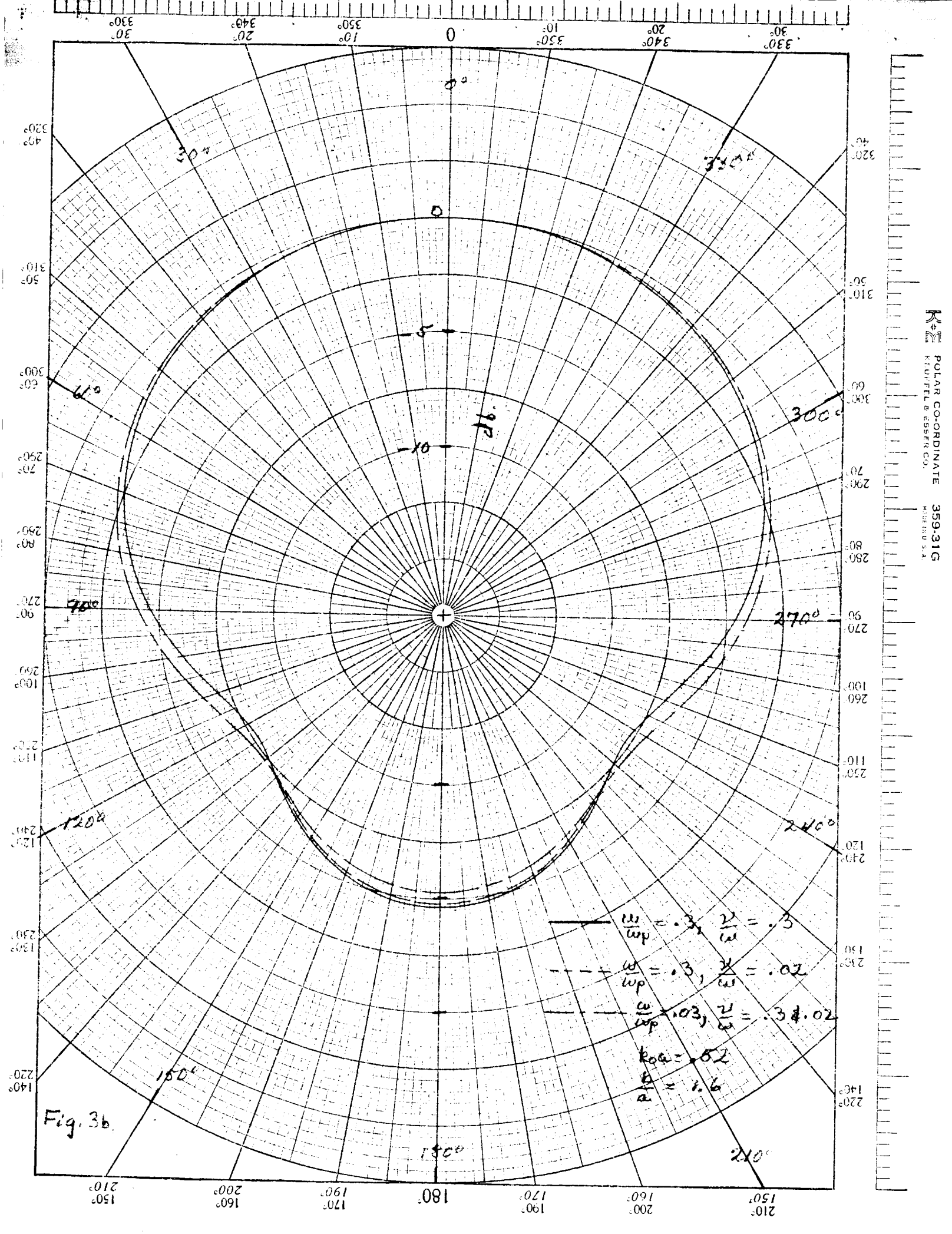
0
30°
60°
90°
120°
150°
180°
210°
240°
270°
300°
330°
-5
-10
$\frac{\omega}{\omega_p} = .3, \frac{\nu}{\omega} = .3$
$\frac{\omega}{\omega_p} = .3, \frac{\nu}{\omega} = .02$
$\frac{\omega}{\omega_p} = .03, \frac{\nu}{\omega} = .3 \& .02$
$k_0 a = .52$
$\frac{b}{a} = 1.6$
POLAR CO-ORDINATE
KEUFFEL & ESSER CO.
359-31G

Fig. 3b

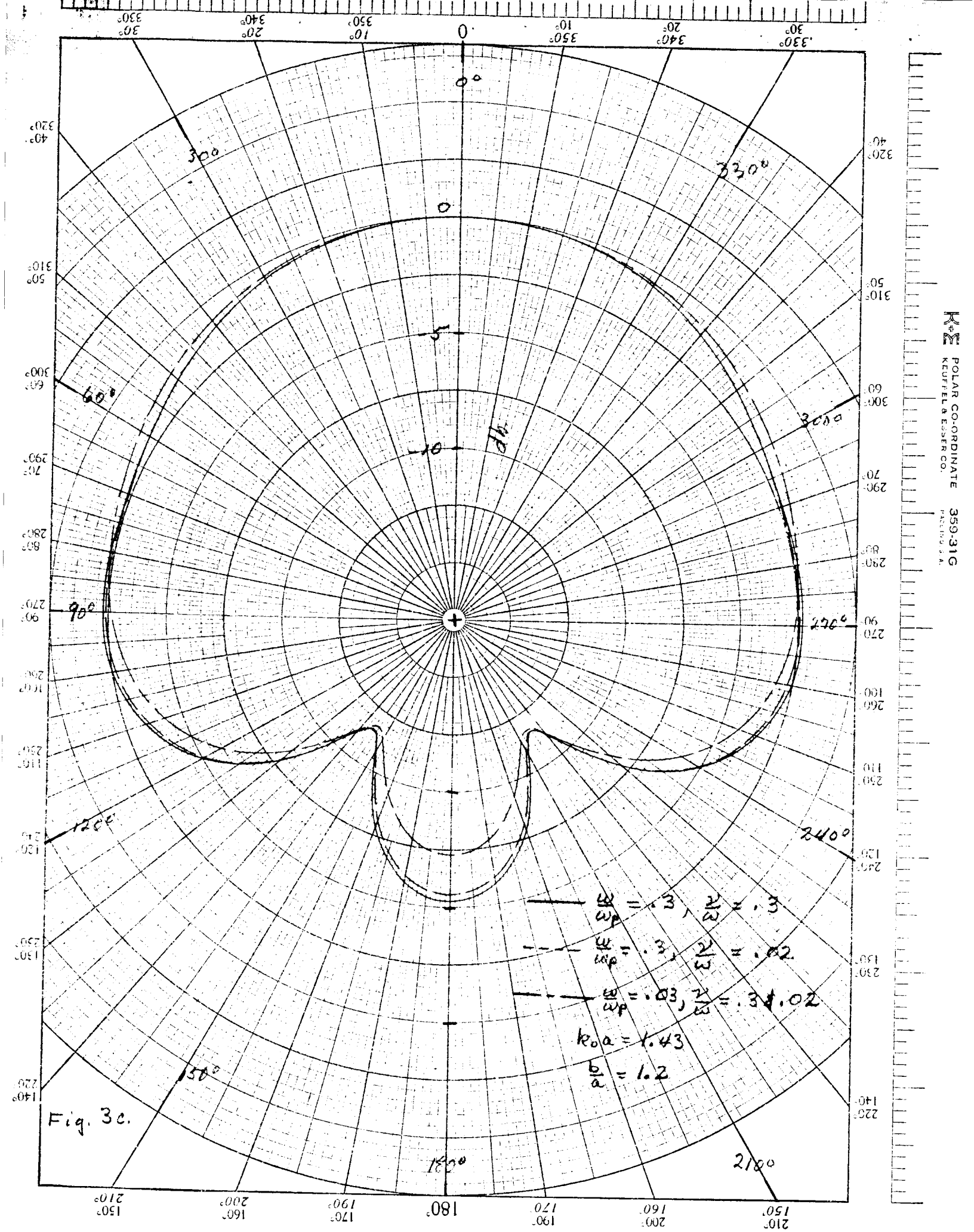
0°
30°
60°
90°
120°
150°
180°
210°
240°
270°
300°
330°
-5
-10
dB
$\frac{\omega}{\omega_p} = .3, \frac{\nu}{\omega} = .3$
$\frac{\omega}{\omega_p} = .3, \frac{\nu}{\omega} = .02$
$\frac{\omega}{\omega_p} = .03, \frac{\nu}{\omega} = .3 \& .02$
$k_0 a = 1.43$
$\frac{b}{a} = 1.2$

Fig. 3c.

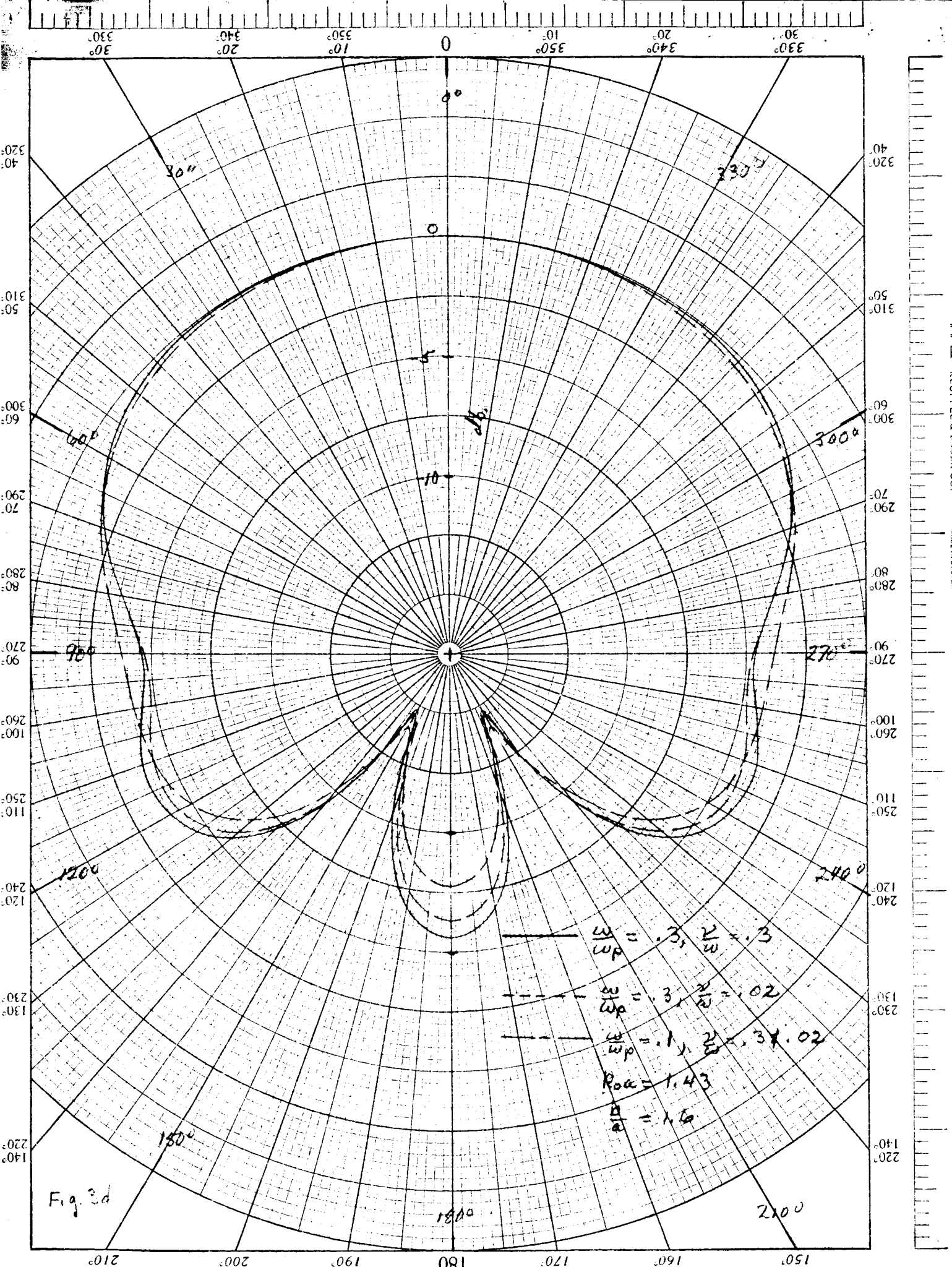

Fig. 3d

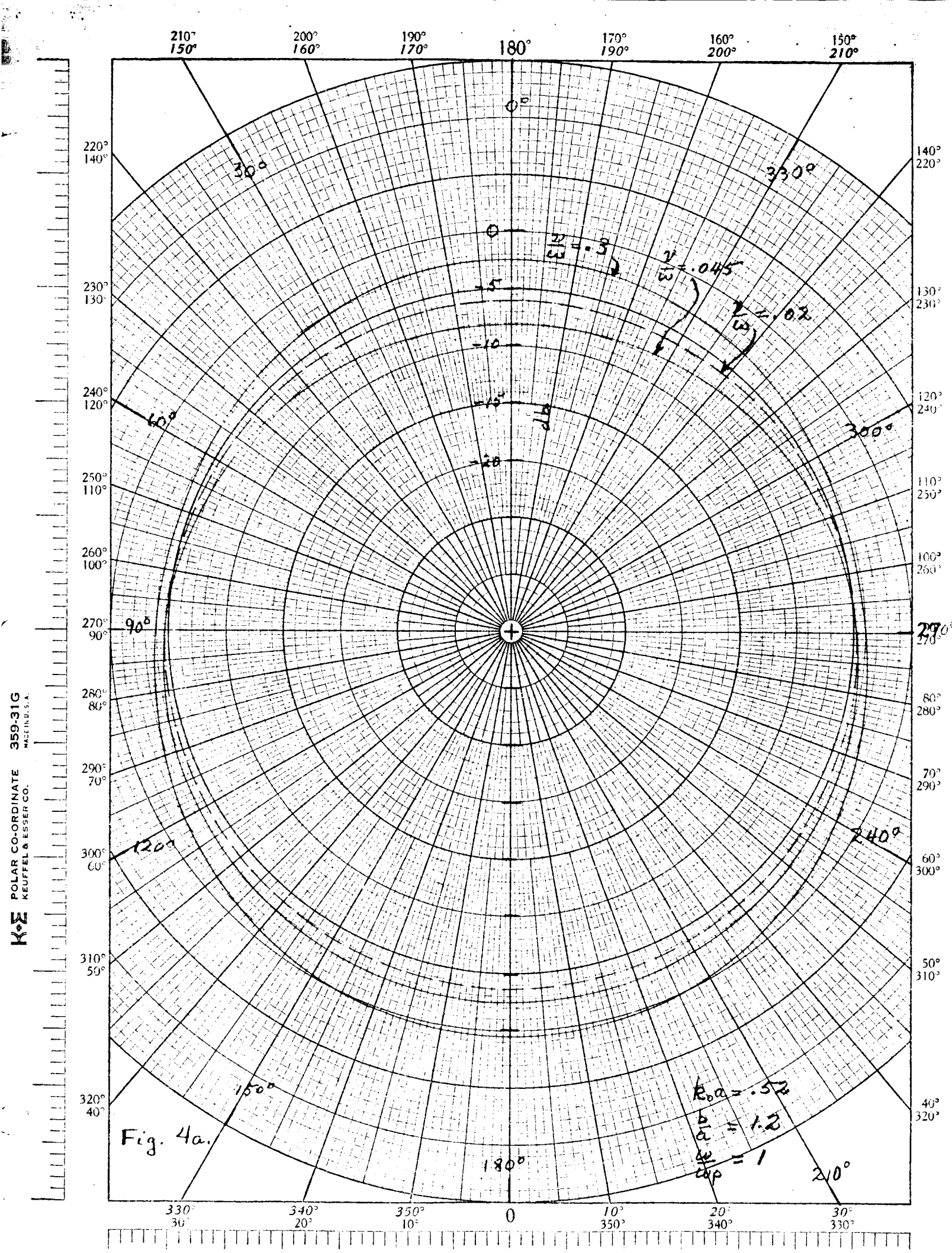
210° 150°
200° 160°
190° 170°
180°
170° 190°
160° 200°
150° 210°
220° 140°
230° 130°
240° 120°
250° 110°
260° 100°
270° 90°
280° 80°
290° 70°
300° 60°
310° 50°
320° 40°
330° 30°
340° 20°
350° 10°
0
10° 350°
20° 340°
30° 330°
140° 220°
130° 230°
120° 240°
110° 250°
100° 260°
80° 280°
70° 290°
60° 300°
50° 310°
40° 320°
30°
60°
90°
120°
150°
180°
210°
240°
270°
300°
330°
0
-5
-10
-15
-20
dB
$\frac{v}{\omega} = .3$
$\frac{v}{\omega} = .045$
$\frac{v}{\omega} = .02$
$k_0 a = .5\pi$
$\frac{b}{a} = 1.2$
$\frac{\omega}{\omega_p} = 1$
Fig. 4a.
POLAR CO-ORDINATE 359-31G
KEUFFEL & ESSER CO.
MADE IN U.S.A.

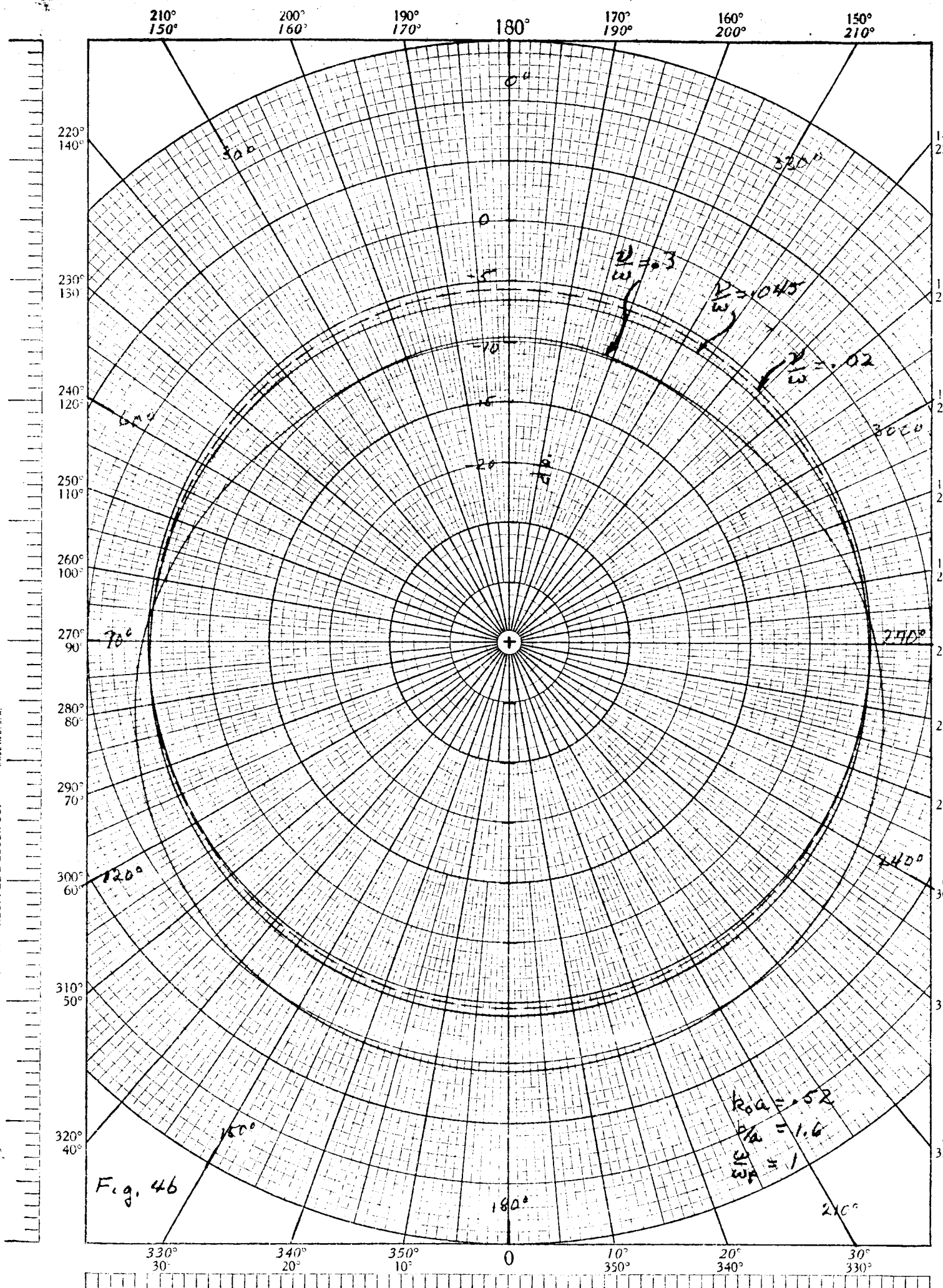

Fig. 46

POLAR CO-ORDINATE 359-31G
KEUFFEL & ESSER CO. MADE IN U.S.A.
K&E

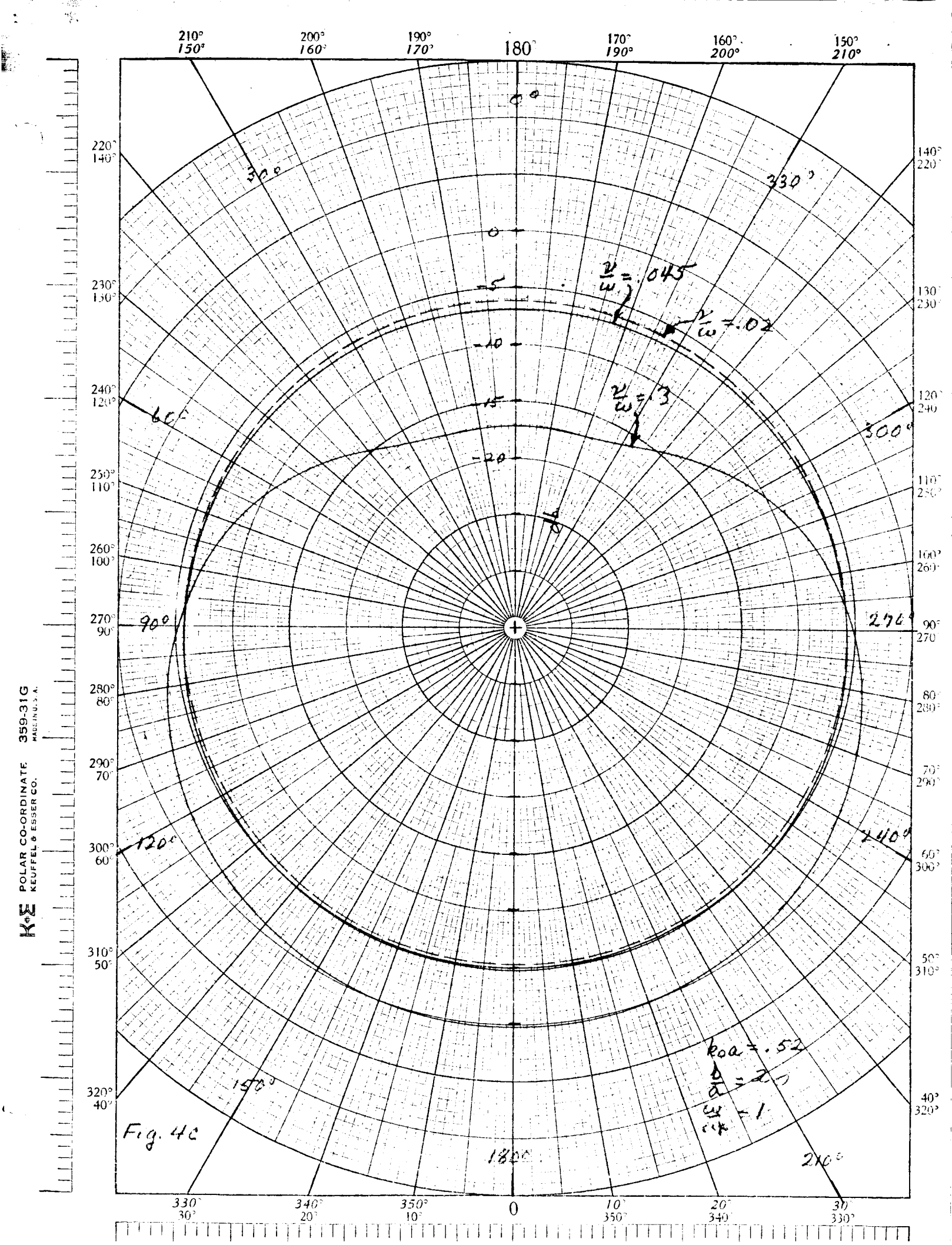
210° 150°
200° 160°
190° 170°
180°
170° 190°
160° 200°
150° 210°
220° 140°
230° 130°
240° 120°
250° 110°
260° 100°
270° 90°
280° 80°
290° 70°
300° 60°
310° 50°
320° 40°
330° 30°
340° 20°
350° 10°
0
10° 350°
20° 340°
30° 330°
140° 220°
130° 230°
120° 240°
110° 250°
100° 260°
90° 270°
80° 280°
70° 290°
60° 300°
50° 310°
40° 320°
30°
0°
-5
-10
-15
-20
0
60°
90°
120°
150°
180°
210°
240°
270°
300°
330°
$\frac{\nu}{\omega} = .045$
$\frac{\nu}{\omega} = .02$
$\frac{\nu}{\omega} = .3$
$ka = .52$
$\frac{b}{a} = 2.0$
$\frac{\omega}{c/a} = 1$
Fig. 4c
K+E POLAR CO-ORDINATE 359-31G
KEUFFEL & ESSER CO.
MADE IN U.S.A.

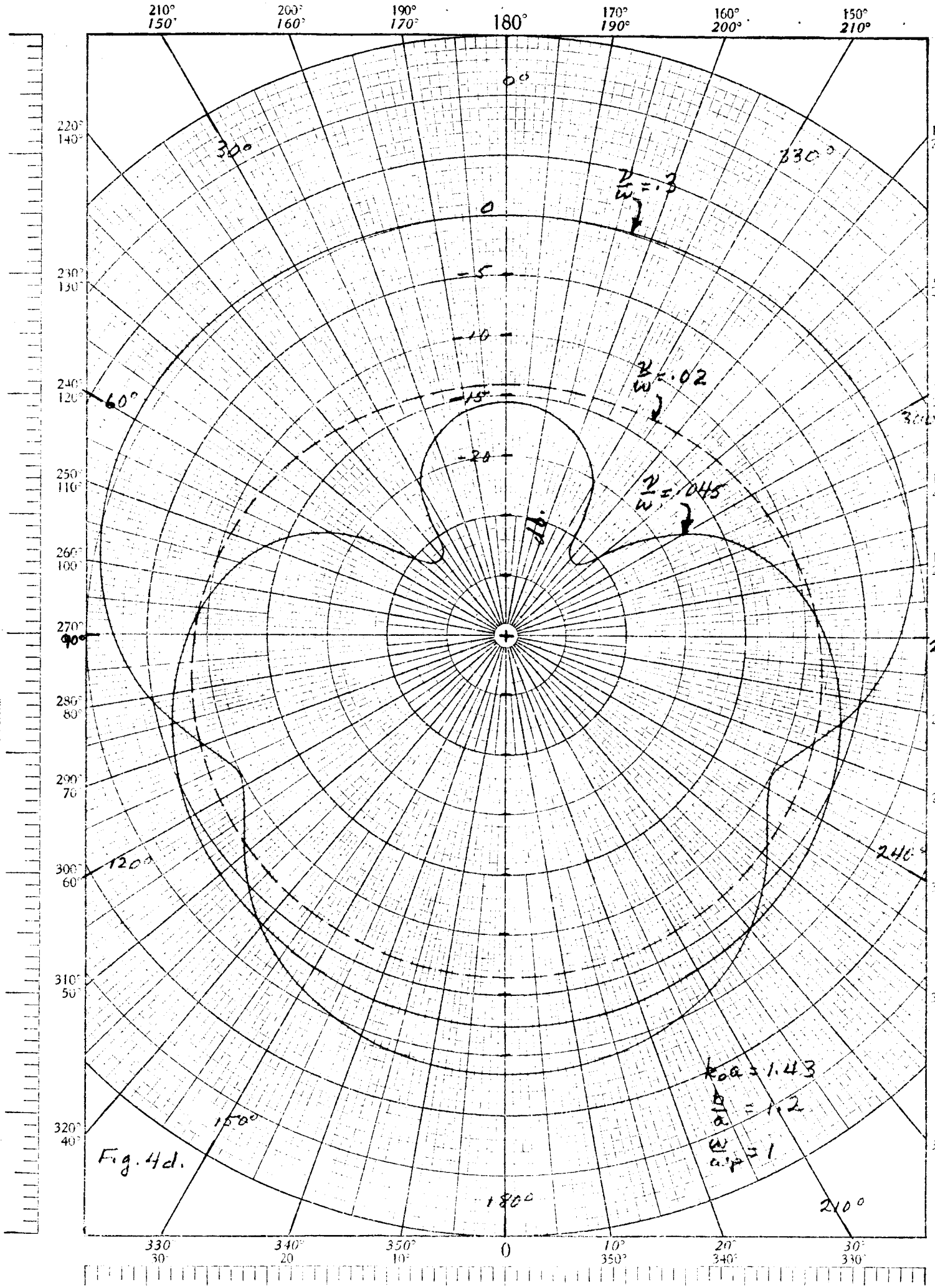
180°
0°
30°
330°
60°
300°
90°
270°
120°
240°
150°
210°
0
-5
-10
-15
-20
$\frac{y}{w} = .3$
$\frac{y}{w} = .02$
$\frac{y}{w} = .045$
$k_0 a = 1.43$
$\frac{b}{a} = 1.2$
$\frac{w}{a \cdot p} = 1$
POLAR CO-ORDINATE
KEUFFEL & ESSER CO.
359-31G

Fig. 4d.

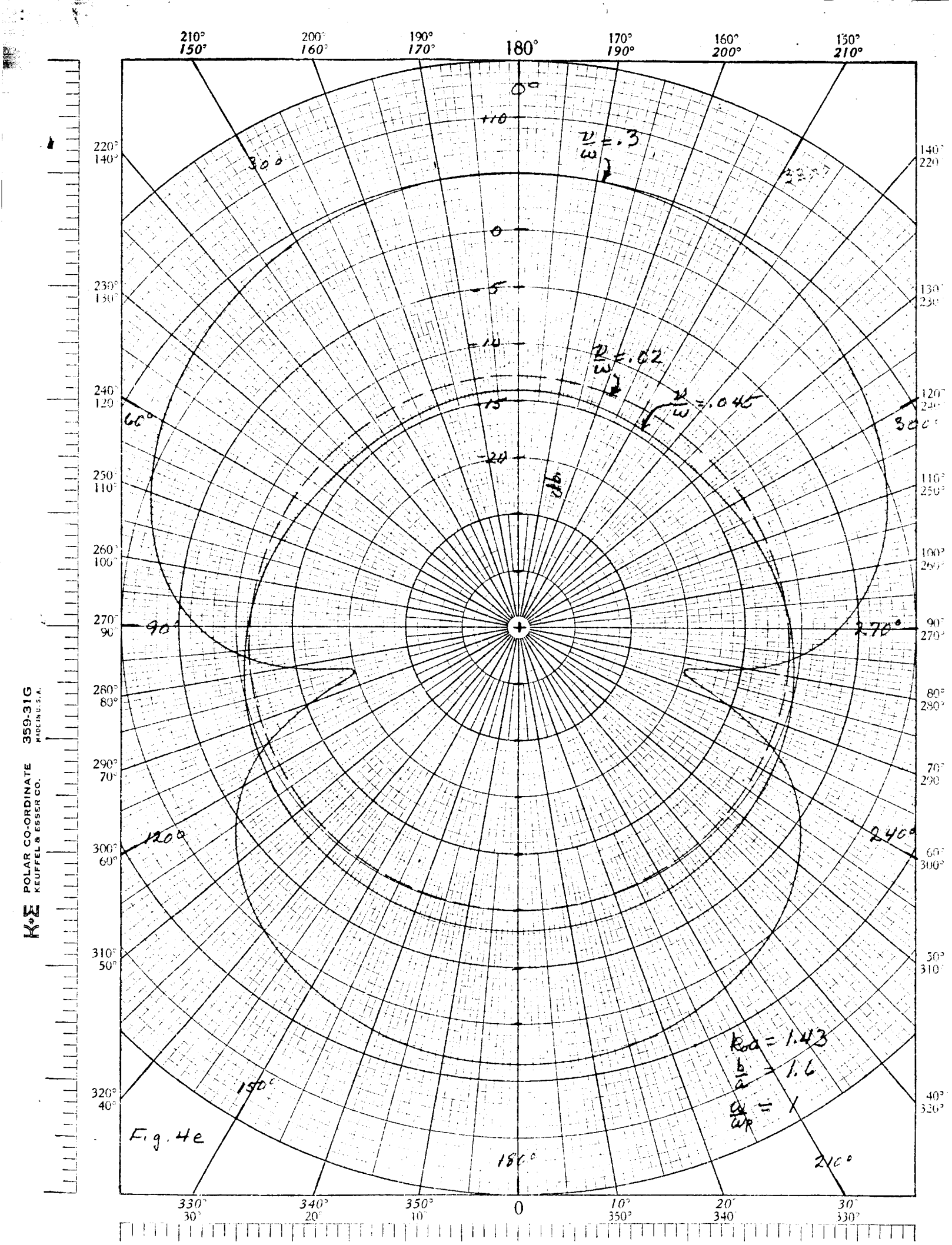
210° 150°
200° 160°
190° 170°
180°
170° 190°
160° 200°
150° 210°
0°
+10
0
-5
-10
-15
-20
db
$\frac{\nu}{\omega} = .3$
$\frac{\nu}{\omega} = .02$
$\frac{\nu}{\omega} = .045$
300°
60°
90°
270°
120°
240°
150°
210°
180°
0
330° 30°
340° 20°
350° 10°
10° 350°
20° 340°
30° 330°
220° 140°
230° 130°
240° 120°
250° 110°
260° 100°
270° 90°
280° 80°
290° 70°
300° 60°
310° 50°
320° 40°
140° 220°
130° 230°
120° 240°
110° 250°
100° 260°
90° 270°
80° 280°
70° 290°
60° 300°
50° 310°
40° 320°
$ka = 1.43$
$\frac{b}{a} = 1.6$
$\frac{\omega}{\omega_p} = 1$
Fig. 4e
POLAR CO-ORDINATE
KEUFFEL & ESSER CO.
359-31G
MADE IN U.S.A.

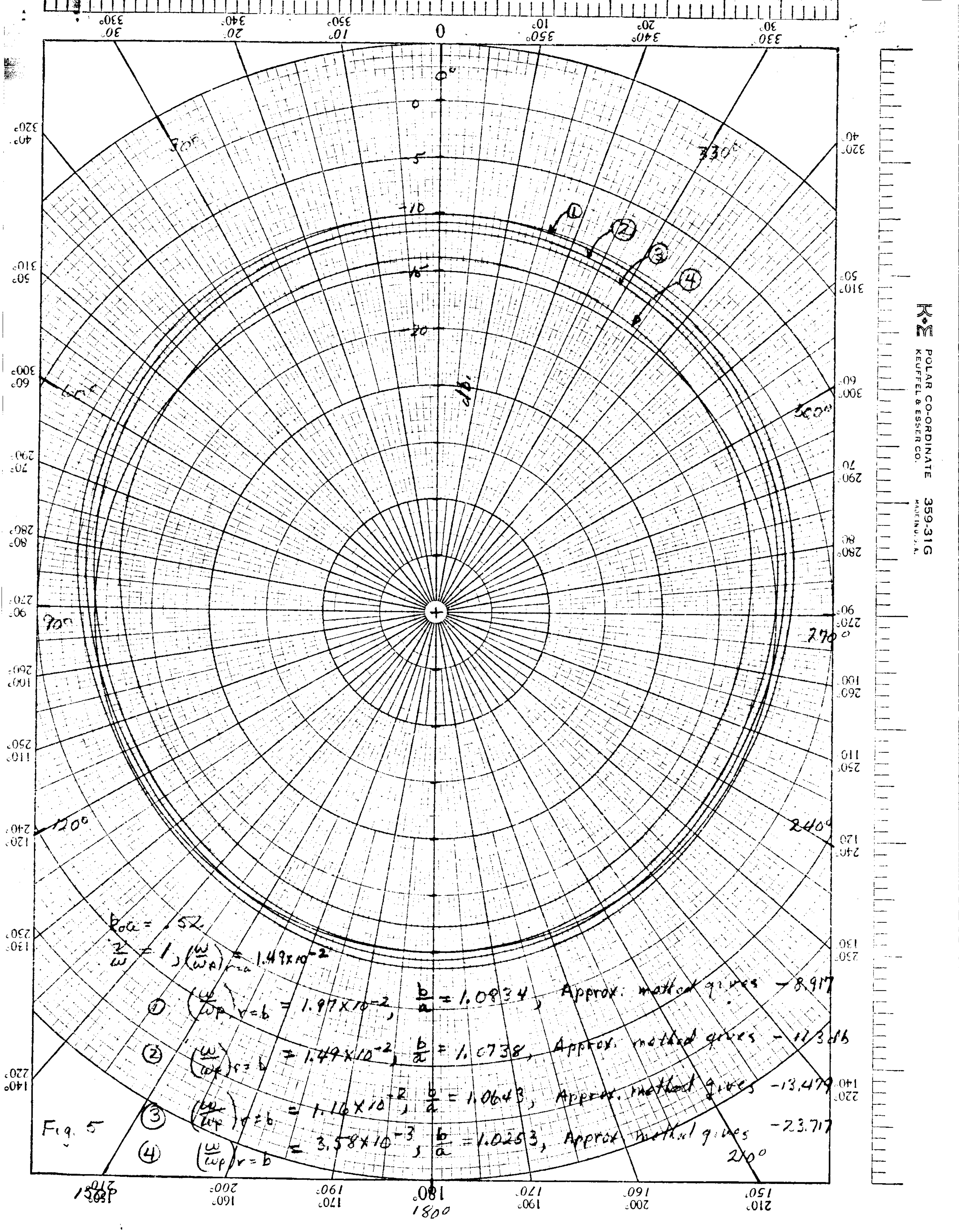

0°
0
5
10
15
20
dB
①
②
③
④
30°
330°
60°
300°
90°
270°
120°
240°
210°
150°
180°
$\rho_0 a = .52$
$\frac{\nu}{\omega} = 1$, $\left(\frac{\omega}{\omega_p}\right)_{r=a} = 1.49\times10^{-2}$
① $\left(\frac{\omega}{\omega_p}\right)_{r=b} = 1.97\times10^{-2}$, $\frac{b}{a} = 1.0834$, Approx. method gives −8.917
② $\left(\frac{\omega}{\omega_p}\right)_{r=b} = 1.49\times10^{-2}$, $\frac{b}{a} = 1.0738$, Approx. method gives −11.3 db
③ $\left(\frac{\omega}{\omega_p}\right)_{r=b} = 1.16\times10^{-2}$, $\frac{b}{a} = 1.0643$, Approx. method gives −13.479
④ $\left(\frac{\omega}{\omega_p}\right)_{r=b} = 3.58\times10^{-3}$, $\frac{b}{a} = 1.0253$, Approx. method gives −23.717
POLAR CO-ORDINATE KEUFFEL & ESSER CO. 359-31G MADE IN U.S.A.

Fig. 5

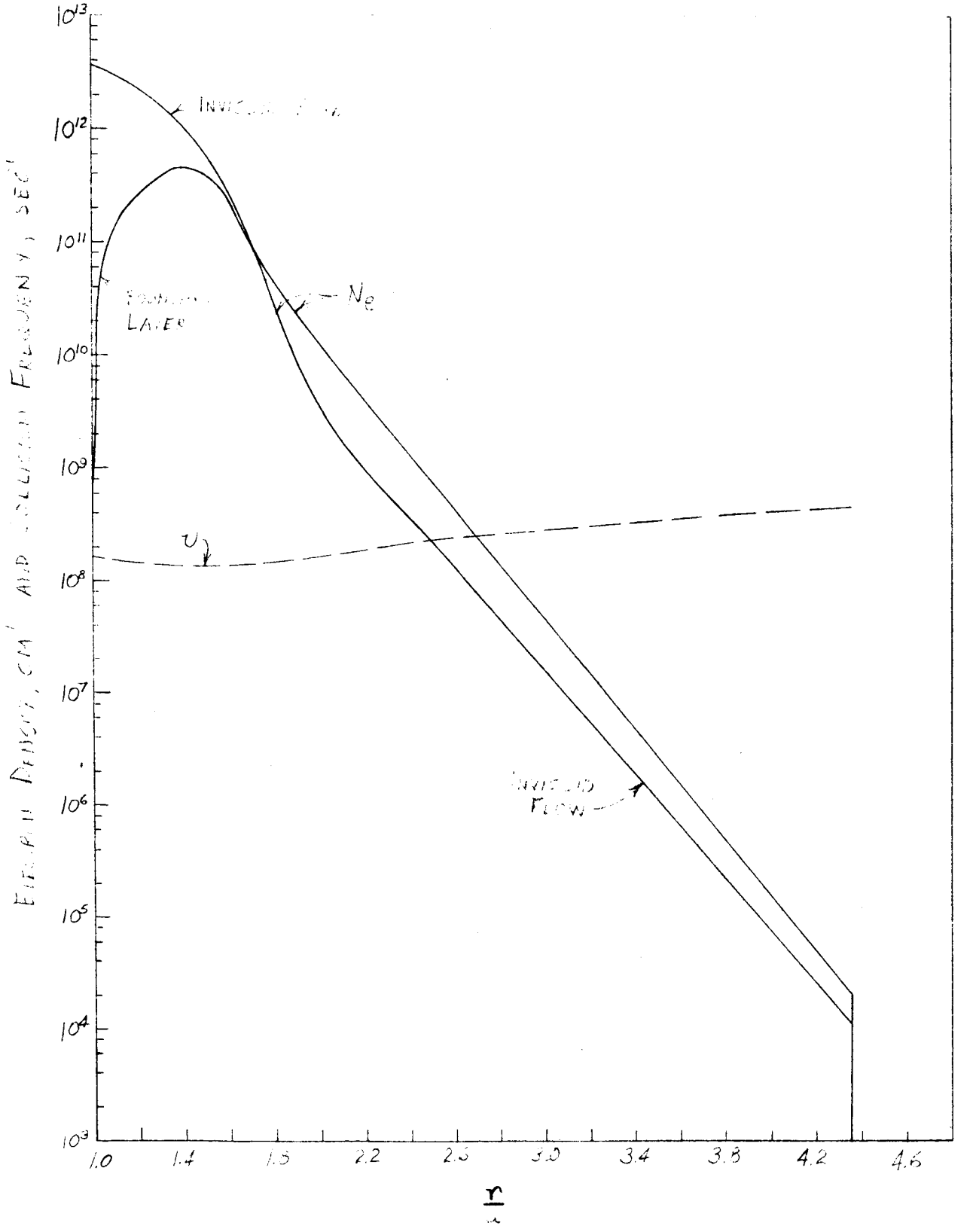
10^{13}
10^{12}
10^{11}
10^{10}
10^{9}
10^{8}
10^{7}
10^{6}
10^{5}
10^{4}
10^{3}
N_e
v_j
1.0
1.4
1.8
2.2
2.6
3.0
3.4
3.8
4.2
4.6
$\frac{r}{a}$

Fig. 6

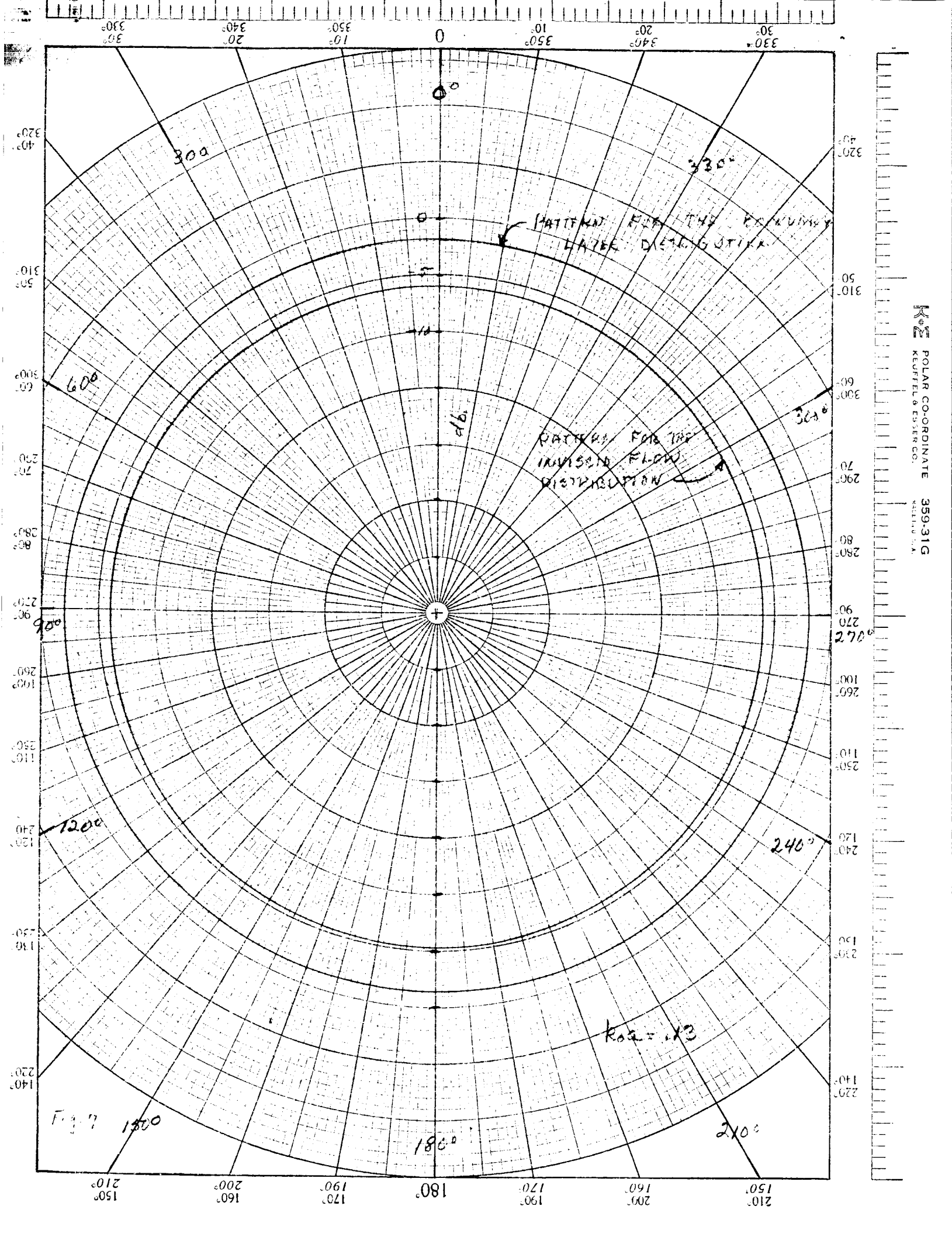
PATTERN FOR THE EQUIVALENT LAYER DIFFRACTOR
PATTERN FOR THE INVISCID FLOW DISTRIBUTION
dB
0°
30°
60°
90°
120°
150°
180°
210°
240°
270°
300°
330°
K&E POLAR CO-ORDINATE 359-31G
KEUFFEL & ESSER CO.

Fig 7

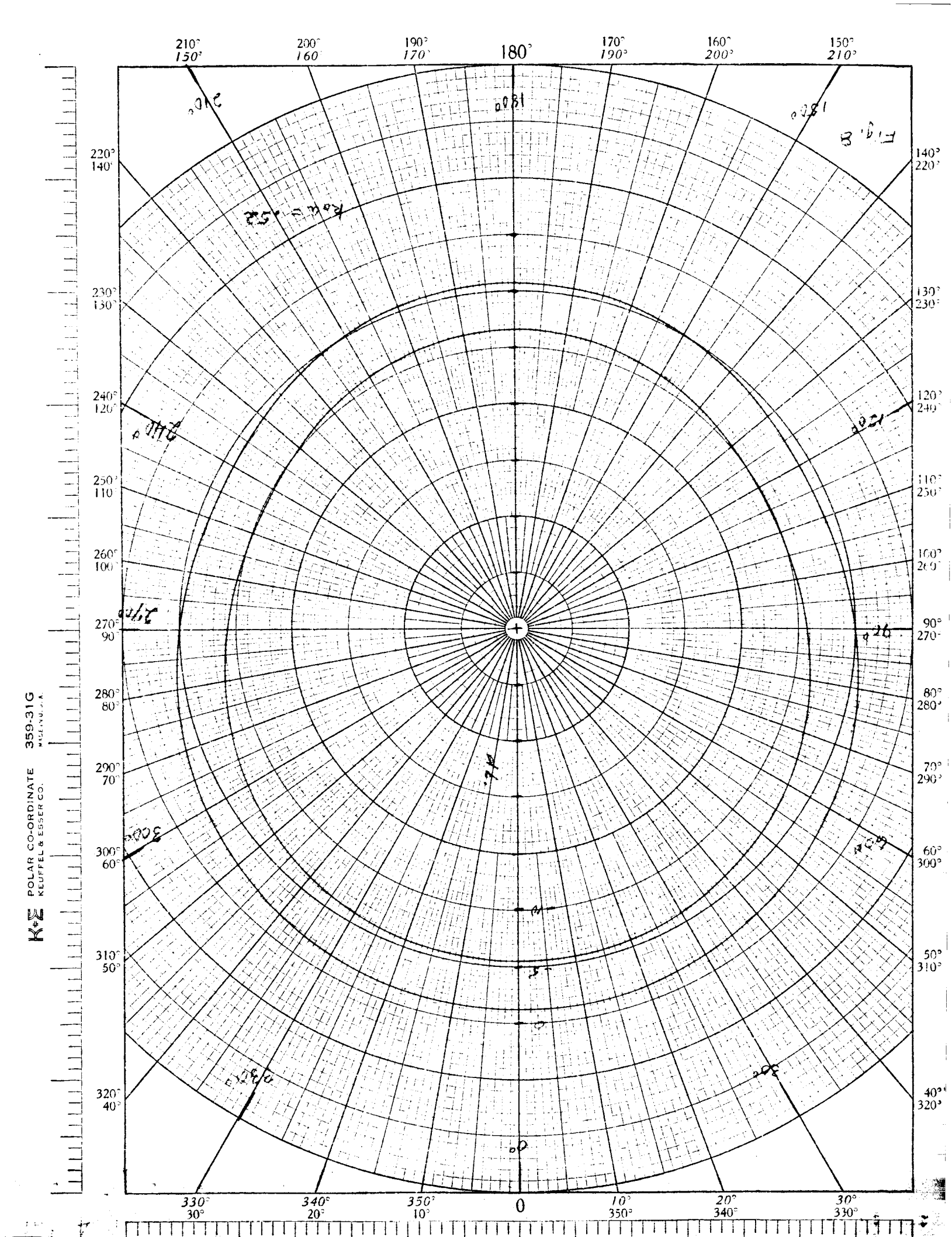
210° 150°
200° 160°
190° 170°
180°
170° 190°
160° 200°
150° 210°
220° 140°
230° 130°
240° 120°
250° 110°
260° 100°
270° 90°
280° 80°
290° 70°
300° 60°
310° 50°
320° 40°
330° 30°
340° 20°
350° 10°
0
10° 350°
20° 340°
30° 330°
140° 220°
130° 230°
120° 240°
110° 250°
100° 260°
90° 270°
80° 280°
70° 290°
60° 300°
50° 310°
40° 320°
POLAR CO-ORDINATE
KEUFFEL & ESSER CO.
359-31G